Journal of Materials Science & Technology 126 (2022) 252–265

Contents lists available at ScienceDirect

Journal of Materials Science & Technology

journal homepage: www.elsevier.com/locate/jmst

Research Article

Coupling a titanium dioxide based heterostructure photoanode with electroless-deposited nickel-phosphorus alloy coating on magnesium alloy for enhanced corrosion protection

Yue Liu[a,1], Feng Peng[b,1], Guang-Ling Yang[a,1], Zhi-Hui Xie[a,*], Wenxin Dai[c], Yuejun Ouyang[d], Liang Wu[e], Chuan-Jian Zhong[f,*]

[a] Chemical Synthesis and Pollution Control Key Laboratory of Sichuan Province, College of Chemistry and Chemical Engineering, China West Normal University, Nanchong 637002, China
[b] Medical Research Center, Department of Orthopedics, Guangdong Provincial People's Hospital, Guangdong Academy of Medical Sciences, Guangzhou 510080, China
[c] State Key Laboratory of Photocatalysis on Energy and Environment, Fuzhou University, Fuzhou 350116, China
[d] Hunan Engineering Laboratory for Preparation Technology of Polyvinyl Alcohol (PVA) Fiber Material, Huaihua University, Huaihua 418000, China
[e] College of Materials Science and Engineering/National Engineering Research Center for Magnesium Alloys, Chongqing University, Chongqing 400044, China
[f] Department of Chemistry, State University of New York at Binghamton, Binghamton, NY, 13902, United States

ARTICLE INFO

Article history:
Received 6 November 2021
Revised 28 January 2022
Accepted 24 February 2022
Available online 21 April 2022

Keywords:
Magnesium alloy
Corrosion
Nickel coating
Electroless
Photoelectrochemical cathodic protection

ABSTRACT

The utilization of photoelectrochemical cathodic protection (PECCP) enables an indirect corrosion protection of metals with low self-corrosion potential by introducing a metallic nickel interlayer. However, the ability to enhance the PECCP efficiency remains challenging because of the inherent property of the semiconductor. Herein, this ability is demonstrated by coupling a covalent organic framework (TpBD) decorated TiO_2 photoanode (TiO_2/TpBD) with nickel coating on magnesium alloy for an effective corrosion protection. The composite photoanode showed direct PECCP for the nickel interlayer and indirect corrosion protection of the magnesium alloy. The composite structure of the nanotube array and the covalent organic framework for the photoanode were confirmed by field emission scanning electron microscopy (FESEM), transmission electron microscopy (TEM), and X-ray photoelectron spectroscopy (XPS). The enhanced photoelectrochemical conversion capability and PECCP performance of the nickel-coated Mg alloy were evidenced by the results from electrochemical and photoelectrochemical measurements including Mott-Schottky curves, photoinduced potential variations, and electrochemical impedance spectroscopy (EIS). Lastly, a corrosion protection mechanism is proposed, where the enhanced PECCP efficiency is attributed to the formation of a direct Z-scheme heterojunction, which is substantiated by the results from valence band (VB) XPS and electron spin resonance characterizations.

1. Introduction

Globally, the total annual estimated direct economic losses caused by metal corrosion account for about 3% - 5% of the global gross product, which is far greater than the sum of losses from weather-related disasters and other types of accidents [1]. The specific hazard includes material wasting, environmental pollution, and severe engineering safety accidents, which are detrimental to the energy-efficient economy and sustainable environment [1,2]. Many technical and nontechnical preventive strategies have been developed to minimize the impact of corrosion [3]. The most frequently used conventional techniques for preventing and controlling corrosion include design of corrosion-resistant alloys, plastics, and polymers [4–10], deposition of organic and inorganic films (such as chemical conversion [11–18], layered double hydroxide [19–27], anodic and plasma electrolytic oxidation [28,29], and metallic protective coatings [30–35]), addition of corrosion inhibitors into corrosive environments [22,36], and traditional cathodic protection [37,38]. These corrosion protection technologies have their advantages and disadvantages, but all need extra consumption of resources and energy [39].

At the end of the 20th century, a new corrosion protection technique called semiconductor photoanode-based cathodic pro-

* Corresponding authors.
E-mail addresses: zhxie@cwnu.edu.cn (Z.-H. Xie), cjzhong@binghamton.edu (C.-J. Zhong).
[1] These authors contributed equally to this work.

https://doi.org/10.1016/j.jmst.2022.02.049
1005-0302/

tection, prevalently known as photoelectrochemical cathodic protection (PECCP) or photogenerated cathodic protection today, was proposed and has received considerable attention in the community of corrosion and protection in recent years. A key attribute of the PECCP technology is the unlimited availability of solar energy compared to conventional cathodic protection that needs external current and sacrificial anodes. PECCP technology is energy-saving and economical and is regarded as a potential environmentally benign alternative to traditional cathodic protection [2]. The PECCP works by generating photogenerated electrons utilizing n-type semiconductors under light irradiation to polarize the potential of the protected metal to a sufficient negative range, achieving thermodynamic stability and protection of metals from degradation. According to the photogenerated electron transfer mechanism in the PECCP process, a lower conduction band (CB) potential for the semiconductor needs to be generated in terms of the self-corrosion potential (E_c) of the protected metal. This mechanism of the PECCP makes it impossible for applications in direct cathodic polarization of metals with a very low E_c, such as magnesium (Mg) alloy that has an E_c value of about −1.5 V vs. SCE in a 3.5 wt.% NaCl solution [40]. This is because the CB potentials of the presently known semiconductor materials are not negative enough. This issue could be addressed by introducing an inert nickel interlayer with high E_c between the substrate and a Cu_2O semiconductor photoanode to enable an indirect pathway for the protection of Mg alloy from corrosion [1]. However, the attempt was unsatisfactory because the photoinduced potential drop was as low as 110 mV due to the limitation of the inherent properties of Cu_2O semiconductors [1].

In this work, we demonstrate the improvement of the direct PECCP performance of the photoanode to the nickel layer on the Mg alloy substrate by exploring advanced modification of semiconductor composite. As an n-type semiconductor with merits of nontoxicity, low cost, and chemical stability, TiO_2 photoanode has been studied extensively and demonstrated applicability in PECCP of several metals, including 304 stainless steels [2]. However, TiO_2 only responds to the near ultraviolet (3% - 5% power of solar light) owing to the wide bandgap (E_g = 3.2 eV), which limits the effective utilization of the solar energy during the PECCP process [2]. Recent studies have demonstrated that doping by metal or nonmetal element, decoration by metal oxide, and compositing with organic frameworks are viable ways to shift the response range of TiO_2 to visible light and thus improve the light absorption and photochemical activities [41]. Among them, covalent organic frameworks have gathered significant interest owing to the ordered structure and extended π-π conjugation that can reduce charge recombination and facilitate charge transport [41,42]. Photocatalytic applications of covalent organic frameworks have been studied extensively in organic reactions, pollutant degradation, H_2 generation, and CO_2 reduction [41], but are scarcely explored in the PECCP field. Our approach involved the preparation of a covalent organic framework TpBD decorated TiO_2 photoanode for the direct PECCP and the preparation of a nickel interlayer with a very low E_c for the indirect corrosion protection to Mg alloy. The morphology, structure, and composition of the as-prepared composite and coating were characterized. The corresponding light absorption, photoelectrochemical conversion, and PECCP performance were tested. Lastly, a corrosion protection mechanism for the present system is proposed, along with discussion of its potential implications.

2. Experimental section

2.1. Preparation of Mg/Ni electrode and TiO_2/TpBD photoanode

The chemical reagents used in the experiments were purchased from Aladdin Industry Co., Ltd. or Sinopharm Chemical Reagents Co., Ltd. The reagents are analytical grade and were not further purified. The nickel-coated Mg alloy (Mg/Ni) was obtained by the electroless nickel plating method. Briefly, AZ31 Mg alloy sheets with a dimension of 2.0 × 3.0 × 0.2 cm^3 were firstly polished by SiC sandpapers (1200 grit), and degreased in an alkaline solution. Then, the substrates were pickled and activated in a phosphoric acid solution (≥ 85.0%, 400 cm^3 dm^{-3}) and hydrofluoric solution (≥ 40.0%, 350 cm^3 dm^{-3}), respectively. After that, the substrates were immersed in a preheated electroless nickel plating bath to form a Ni-P coating on the Mg alloy. The compositions of the solutions for pretreatment of Mg alloy and electroless nickel plating, and the corresponding conditions are summarized in Table S1. The details of the preparation of nickel coating on Mg alloy can also be found in our recent publications [30,31].

The TiO_2/TpBD photoanode was prepared by potentiostatic anodization: Typically, Ti foils (> 99.999%, 15 mm × 10 mm × 0.25 mm) were sequentially degreased in acetone and ethanol under an ultrasonic condition and deionized water for 20 min. Then, the Ti foils were etched in a solution consisting of NH_4F (0.45 g), H_2O (3 mL), H_2O_2 (6 mL), and HNO_3 (6 mL) to remove surface oxides. After chemical polishing, the samples were cleaned by deionized water and then anodized in an electrochemical cell with a two-electrode system. A Pt foil and the Ti sheet were used as the counter electrode (cathode) and the working electrode (anode), respectively. The anode and cathode (at a distance of 3.0 cm) were immersed in an electrolyte composed of 37.0 mL ethylene glycol, 3.0 mL deionized water, and 0.22 g NH_4F. The voltage for anodization was provided by an electrophoresis device (DYJ-2, Sangli, Nanjing). After anodization, the samples were cleaned by using deionized water and ethanol several times to remove residual electrolytes. The as-prepared samples were annealed at 450 °C for 2 h in a tube furnace at a heating rate of 5 °C min^{-1} to obtain anatase phase TiO_2 nanotube arrays. For writing conveniently, hereinafter, the TiO_2 nanotube arrays are simply referred to as TiO_2. To obtain the best photoelectrochemical performance, the TiO_2 were prepared at different times (30, 90, 60, and 120 min), temperatures (15, 25, 35, and 45 °C), voltages (20, 40, 60, and 80 V), and concentrations of NH_4F (0.1 wt.%, 0.3 wt.%, 0.5 wt.%, and 0.7 wt.%). The photo-induced current density and potential variations for the samples prepared under different reaction conditions are given and discussed in the Supporting Information.

The deposition of the covalent organic framework on the TiO_2 was obtained by a hydrothermal synthesis method at 393 K. Firstly, 1, 3, 5-trimethylbenzene (C_9H_{12}, 15 ml) and 1, 4-dioxane ($C_4H_8O_2$, 15 ml) were mixed and ultrasonically agitated for 20 min in a beaker (50 mL). Then, 1, 3, 5-triformylphloroglucinol (Tp, $C_9H_6O_6$, 6.3 mg), benzidine (BD, $C_{12}H_{12}N_2$, 8.3 mg), and aqueous acetic acid (0.172 mL) were added into the mixture, followed by sonication for 20 min to produce a homogeneous dispersion. The dispersion was then poured into a Teflon-lined stainless-steel autoclave where an anodized TiO_2 foil had been obliquely placed. The autoclave was transferred into an oven and heated at 120 °C for 3 days. Afterward, tangerine precipitates (i.e., TpBD) were formed both on the TiO_2 surface and at the bottom of the Teflon liner. The TpBD-coated TiO_2 was then wrapped with filter paper and extracted with acetone at 88 °C for 24 h in a 250 ml Soxhlet extraction apparatus. Meanwhile, centrifugal separation of the precipitate at the bottom of the Teflon liner by acetone was repeated 5 times. After drying of the acetone-extracted TiO_2 and precipitate in vacuum at 60 °C for 6 h, TiO_2/TpBD photoanode for PECCP to nickel-coated Mg alloy and TpBD powder for characterization were obtained, respectively. The schematic diagram for the fabrication of the TiO_2/TpBD composite photoanode is shown in Fig. 1.

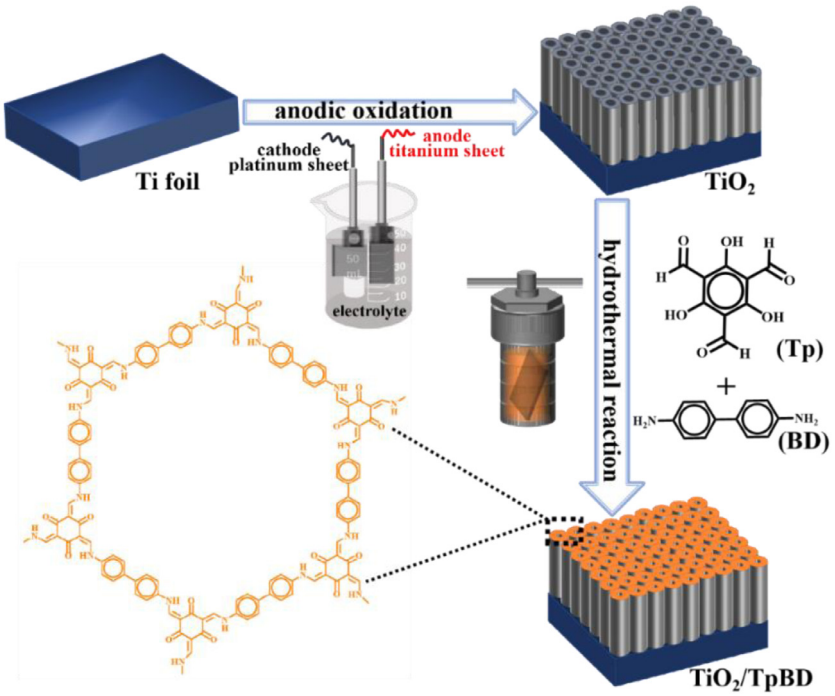

Fig. 1. Schematic diagram for preparation of the TiO_2/TpBD composite photoanode.

2.2. Morphological, structural, and compositional characterizations of the fabricated materials

The surface morphology and microstructure of TiO_2, TpBD, and TiO_2/TpBD were obtained by field emission scanning electron microscopy (FESEM, SU8020, 3 kV, Hitachi), transmission electron microscopy (TEM), and a high-resolution TEM (HRTEM, FEI Tecnai G2 F30, America) with an accelerating voltage of 300 kV. An X-ray energy dispersive spectrometer (EDS) coupled with the SEM was used for qualitative examination of element content and distribution. An X-ray diffractometer (XRD, Bruker D8 Advance, $\lambda = 0.154$ nm, Germany) was used to identify the composition and crystallographic structure of the TpBD with scan speeds of 5° min^{-1} or 1° min^{-1}. X-ray photoelectron spectroscopy (XPS, Thermo Ecalab 250Xi America) was employed to analyze the chemical states of the elements. Functional group information was obtained by Fourier transform infrared spectroscopy (FTIR, Nicolet-6700, America) within the range of 400 - 4000 cm^{-1}. The light absorption performance was acquired by using an ultraviolet-visible diffuse reflectance spectrometer (UV–vis DRS, UV3600, Tsushima, Japan) in the wavelength range of 200 - 800 nm. Electron spin resonance (ESR) spectra were acquired using a Bruker A300–10/12 spectrometer coupled with an N_2 heating set-up operated at 9.85 GHz (modulation frequency = 100 kHz, amplitude = 1.0 G) under visible light irradiation.

2.3. Photoelectrochemical and PECCP performance measurements

All photoelectrochemical and PECCP performance tests were measured by an electrochemical workstation (Gamry, Interface 1010E, America) coupled with a 300 W Xe lamp. A three-electrode system in an electrochemical cell, in which TiO_2/TpBD sample acted as a working electrode, Pt foil acted as a counter electrode, and saturated calomel electrode (SCE) acted as a reference electrode, was used to survey the Mott-Schottky and current density over potential (j - E) curves. The Mott-Schottky curves were measured in dark in an electrolyte containing 0.1 mol L^{-1} Na_2S and 0.2 mol L^{-1} NaOH at a perturbation frequency of 1.0 kHz in the potential range from −0.6 to 1.0 V. The j - E curves were measured from −1.0 to 1.0 V (vs. SCE) with a scan rate of 20 mV s^{-1} under intermittent visible light (the interval is 2 s). The illumination with a power energy density of 150 mW cm^{-2} was achieved by the Xe lamp combined with a 420 nm cutoff filter (PLS-SXE300, Beijing Perfectlight Technology Co., Ltd.).

The PECCP performance was obtained by monitoring the curves of open circuit potential over time (OCP - t) and current density over time (j - t) under intermittent visible light by using a three-electrode system with two electrochemical cells. The TiO_2/TpBD photoanode was immersed in a photoelectrochemical cell containing Na_2S (0.1 mol L^{-1}) and NaOH (0.2 mol L^{-1}), while the Pt foil, SCE, and Mg/Ni sample with an area of 1 cm^2 were exposed to a 3.5 wt.% NaCl solution in a corrosion cell. The corrosion cell and the photoelectrochemical cell were connected by a salt bridge. The TiO_2/TpBD photoanode and the Mg/Ni sample were connected by a copper wire. A more detailed diagram can be found in our previous publication [1]. Also, the system was used to test the electrochemical impedance spectroscopy (EIS) in the frequency range of 100 kHz - 0.01 Hz with a 10 mV AC single. The potentiostatic polarization curves were measured at a potential range of ±0.5 V vs. OCP with a scan rate of 5 mV^{-1}. All tests were performed after 20 min of OCP tests until a stable potential was obtained.

3. Results and discussion

3.1. Morphology, structure, and composition of the fabricated semiconductors

Structural morphologies and elemental compositions of the TiO_2 before and after deposition of TpBD semiconductor are illustrated in Fig. 2. As shown in Fig. 2(a), an ordered nanotube array film with a thickness of 9.0 μm (inset at the bottom left corner) is formed on the Ti foil after anodic oxidation. The outer and inner diameters of the nanotubes are about 148 and 125 nm, respectively, meaning that the average thickness of the nanotube wall is about 11.5 nm. The long nanotubes with large specific surface areas provide many possibilities for optimizing the photoelectrochemical

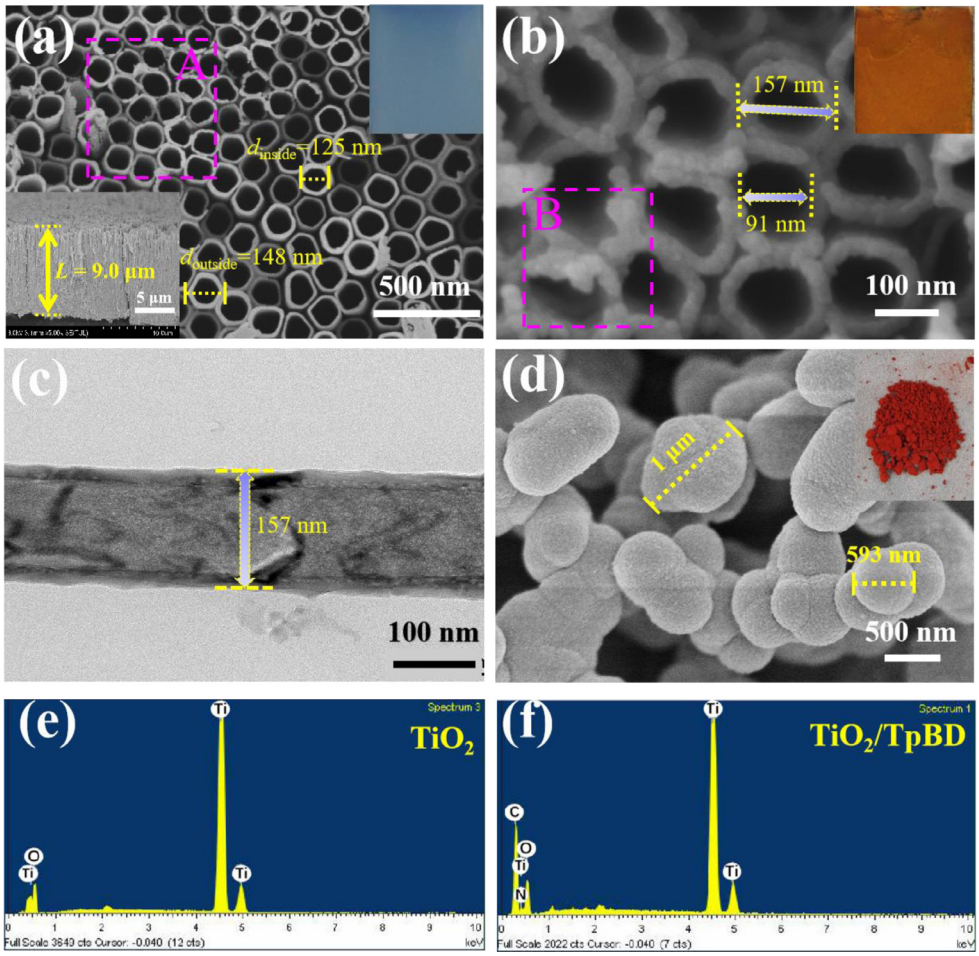

Fig. 2. SEM and TEM images, and EDS spectra of the fabricated semiconductors. The surface morphologies of (a) TiO_2 and (b) TiO_2/TpBD photoanodes, and (d) TpBD powder. (c) TEM image of single TiO_2 nanotube after deposition of TpBD semiconductor. (e) and (f) the corresponding EDS spectra of the square areas (pink dashed squares) in (a) and (b), respectively. Inset at the bottom left corner in (a) is the cross-sectional SEM image of TiO_2 nanotubes. Insets at the top right corner in (a), (b), and (d) are the digital pictures of the corresponding samples.

properties of the photoanode. The color of the photoanode changes from nattier blue to tangerine after deposition of covalent organic framework TpBD on the TiO_2 (i.e., TiO_2/TpBD, Fig. 2(b)). The gaps among the TiO_2 nanotubes are filled up by the formed precipitates. The outer diameters of the nanotubes in the TiO_2/TpBD increase to approximately 157 nm (which is confirmed by the TEM image as illustrated in Fig. 2(c)), while the inner diameters of that decrease to about 91 nm, indicating that the TpBD semiconductor was attached to both the inside and outside surfaces of the TiO_2 nanotubes. The maintained channel structure after deposition of TpBD ensures enough contact between the TpBD semiconductor and the surrounding electrolyte, thus promoting separation efficiency of photogenerated electron-hole pairs (e^--h^+) [43]. The SEM image of the TpBD powder shows aggregated spheres with diameters ranging from several hundreds of nanometers to one micrometer (Fig. 2(d)), which is slightly different from the morphology of the TpBD on the TiO_2 and was also observed in previous studies [44]. The EDS spectra and the corresponding chemical compositions of the TiO_2 and TiO_2/TpBD photoanodes are shown in Fig. 2(e, f) and listed in Table 1, respectively. The EDS result shows that only O and Ti elements with an O/Ti atomic ratio of ~2 exist in the TiO_2 nanotube surface, indicating that high purity TiO_2 film was formed during anodization. After deposition of TpBD, a large amount of carbon (48.96 at.%) is detected in the TiO_2/TpBD sample (TiO_2/TpBD-1 in Table 1), manifesting that some organic species are deposited on the TiO_2 nanotube surface. Since the peaks for titanium and nitrogen are very close and can overlap in the EDS spectra, the composition data for TiO_2/TpBD were also exported after removing the titanium element (TiO_2/TpBD-2 in Table 1). The substantial concentration of nitrogen element confirms the formation of nitrogen-containing organic species on the TiO_2 surface.

Table 1
Chemical compositions of the TiO_2 and TiO_2/TpBD based on EDS spectra (at.%).

	Ti	O	C	N
TiO_2	34.04	65.96	NA	NA
TiO_2/TpBD-1	15.19	35.85	48.96	0
TiO_2/TpBD-2	NA	33.35	53.16	13.49

As shown in Fig. 3(a), the HRTEM micrograph of the TiO_2/TpBD exhibits that both polycrystalline (main) and amorphous (secondary) phases are formed because crystal lattice fringes with different interplanar spacings can be seen in most areas. Meanwhile, crystal lattice fringe cannot be found in some areas (blue dashed circles) in the HRTEM image. The polycrystalline and amorphous structures of the TiO_2/TpBD are also confirmed by the corresponding SAED pattern as shown in Fig. 3(b), which presents bright diffraction spots and diffuse halos. The formation of amorphous covalent polymers is attributed to the insufficient chemical reaction during the hydrothermal process and the rapid precipitation of TpBD [45]. Three typical regions marked by yellow dotted rect-

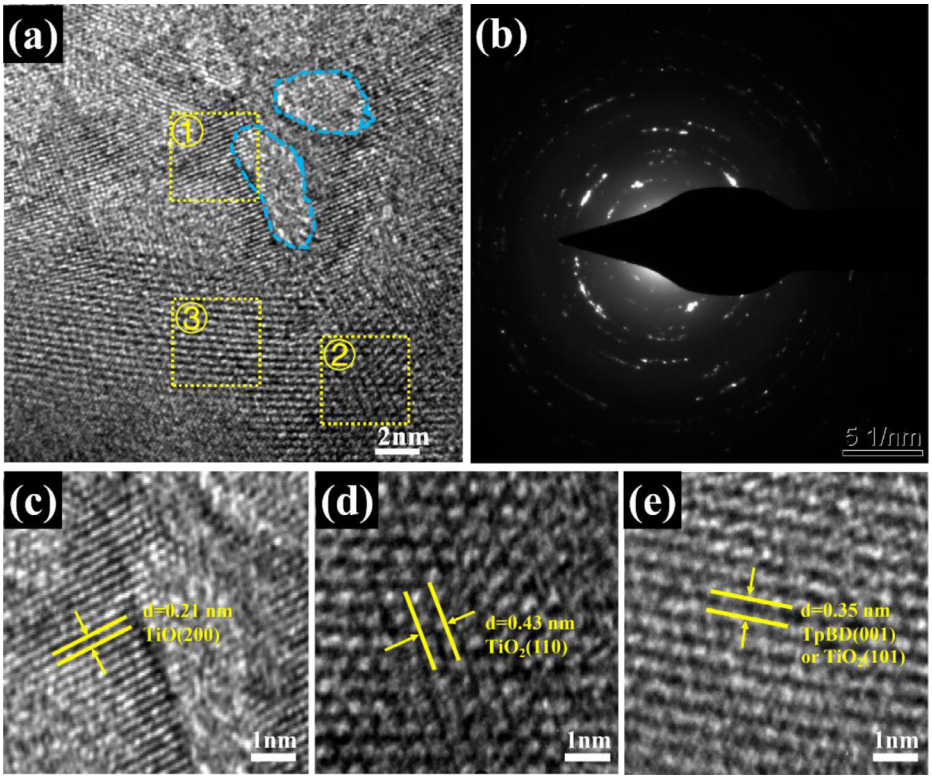

Fig. 3. (a) HRTEM image and (b) corresponding SAED pattern of TiO_2/TpBD. (c)-(e) Magnified lattice fringe images of the areas marked with square ①, ②, and ③ in (a), respectively.

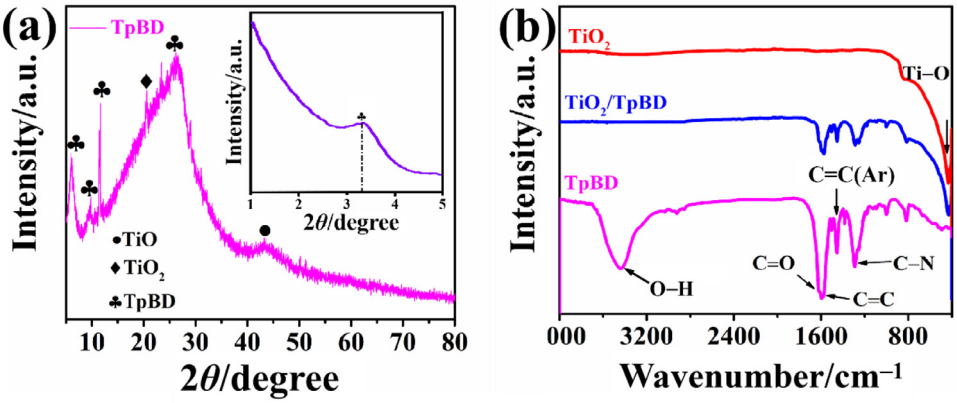

Fig. 4. (a) Powder XRD pattern of the TpBD powder. Inset at the upper right corner is the small-angle XRD pattern of the corresponding sample. (b) FTIR spectra of the TiO_2, TpBD, and TiO_2/TpBD.

angles in Fig. 3(a) are enlarged and illustrated in Fig. 3(c-e) to exhibit the *D*-spacings of different planes in the TEM image more clearly. The crystal lattice fringes with interplanar spacings of 0.21 and 0.43 nm are indexed as (200) and (110) planes for TiO and TiO_2 from the matrix, respectively (Fig. 3(c, d)). Since the lattice distance of (001) plane for TpBD and (101) plane for TiO_2 is very close, it is difficult to assign the well-resolved lattice that has a distance of ~0.35 nm as shown in Fig. 3(e) [46,47].

Powder XRD pattern of the TpBD powder and FT-IR spectra of the fabricated semiconductors are given in Fig. 4 to further identify the crystal structure of the TpBD. The wide-angle XRD pattern and corresponding small-angle XRD pattern (inset) as shown in Fig. 4(a) exhibit obvious reflection peaks at 2θ = 3.39°, 6.13°, 9.85°, and 11.74°, which correspond to (110), (210), (200), and (220) crystal planes of the covalent organic framework TpBD, respectively [47,48]. The broad peak arising from π-π stacking of TpBD layers at 2θ = 26.26° is assigned to (001) crystal plane that has a lattice spacing of 0.35 nm [45,49]. Since a small number of TiO_2 nanotubes broke up, fell off from the Ti foil, and incorporated into the TpBD powder at the bottom of the autoclave during the TpBD synthesis process, peaks for TiO_2 (110) (JCPDS NO:53–0619) and TiO (200) (JCPDS NO:08–0117) are also observed in the XRD pattern.

Fig. 4(b) illustrates the FTIR spectra of the TiO_2, TpBD, and TiO_2/TpBD semiconductors in the wavenumber of 400 - 4000 cm^{-1}. Only a strong adsorption band at 433 cm^{-1} for stretching vibration of Ti-O bond is found in the FTIR spectrum of TiO_2, demonstrating the high purity of the TiO_2 nanotube during anodization [50]. After modification of the TiO_2 with TpBD, the stretching vibration for the Ti-O bond can also be identified clearly (FTIR spectrum for TiO_2/TpBD), indicating that the nanotube structure of the TiO_2 is not destroyed notably during growth of TpBD. More impor-

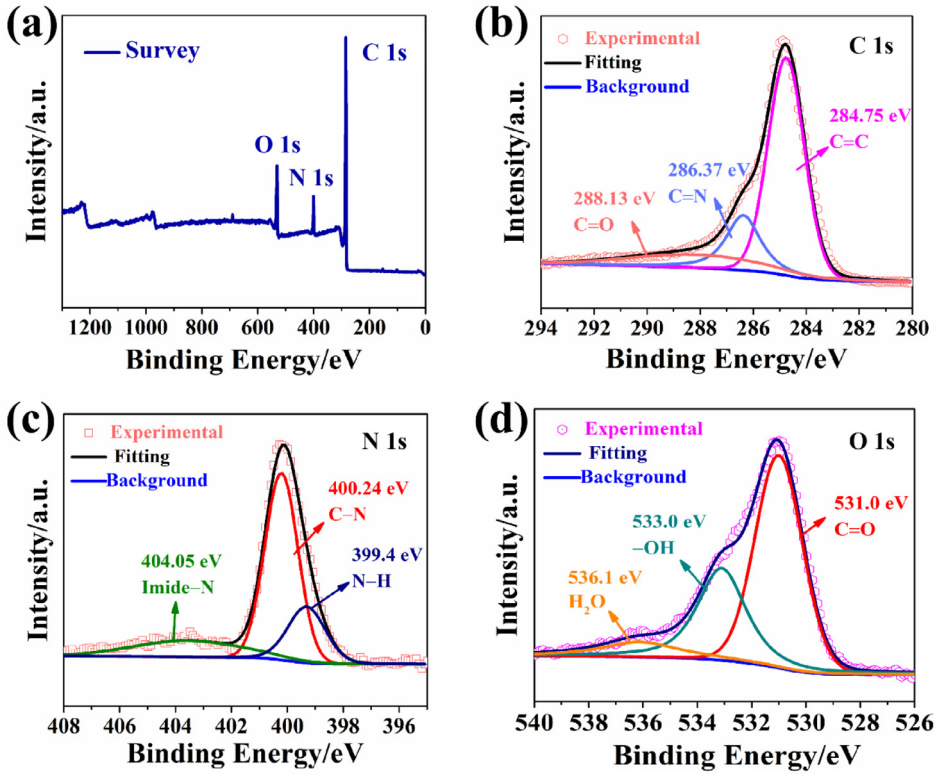

Fig. 5. XPS spectra of the TiO_2/TpBD composite. The (a) survey, high-resolution of (b) C 1s, (c) N 1s, and (d) O 1s spectra.

tantly, several characteristic peaks for TpBD appear in the spectra of TiO_2/TpBD and TpBD samples. For example, strong absorption bands at 1620, 1573, 1452, 1285, and 1000 cm^{-1} are observed in the spectra of both TiO_2/TpBD and TpBD, which are assigned to the stretching of carbonyl C=O [45], C=C, aromatic ring C=C, C–N [51], and C–H bonds of the TpBD, respectively. The broad absorption band at 3300 - 3500 cm^{-1} is attributed to the O–H bending band of adsorbed water on the TpBD powder surface [52,53]. The carbonyl stretching band of Tp should be located at 1643 cm^{-1}, while it is not observed in the FTIR spectra, manifesting that the Tp monomers were consumed completely during the condensation reaction process [49,54].

Fig. 5 shows the chemical composition of the TiO_2/TpBD and corresponding high-resolution XPS spectra for C 1s, N 1s, and O 1s. Since the detection depth of the XPS technique is only several nanometers, and a considerable amount of TpBD has attached to the inside and outside surfaces of the TiO_2 nanotubes, peaks for C (284 eV), N (400 eV), and O (531 eV) elements but no Ti element are detected in the full scan spectrum (Fig. 5(a)) [55]. The C 1s can be divided into three different peaks that are indexed as C=C (284.75 eV), C=N (286.37 eV), and C=O (288.13 eV) bonds of TpBD (Fig. 5(b)) [56,57]. In the N 1s spectrum (Fig. 5(c)), three split peaks located at 399.4, 400.24, and 404.05 eV are assigned to N–H, C–N bonds, and polyimide nitrogen (imide-N) from organic polymer byproduct [56,58]. The appearance of imide-N is attributed to the tautomer formed by imines from BD and enamines from TpBD during the synthesis [57]. In the O 1s spectrum (Fig. 5(d)), three split peaks located at 531.0, 533.0, and 536.1 eV contribute to C=O bonding, chemically adsorbed −OH, and water molecules, respectively [58]. In short, based on the morphological, structural, and compositional characterizations, it can be concluded that the TpBD polymer with a covalent organic framework structure was synthesized and is loaded successfully on the TiO_2 nanotube surface.

3.2. Light absorption and photoelectrochemical conversion performances of the prepared semiconductors

The photoelectrochemical performances of pure TiO_2 and TiO_2/TpBD composite photoanodes are shown in Fig. 6. As shown in Fig. 6(a), the UV–vis spectrum of the TiO_2 photoanode in the wavelength ranging from 200 to 800 nm indicates that pure TiO_2 has strong absorption mainly in the UV region less than 380 nm, with a light absorption threshold of 398 nm, owing to the inherent bandgap of TiO_2 (E_g = 3.2 eV) based on the calculation of the Kubelka-Munk formula and Tauc plot (Fig. 6(b)) [59,60]. The spectrum of the TpBD photoanode exhibits much broader and stronger absorption in both the UV and visible light regions in contrast to the TiO_2 photoanode, which is ascribed to the significant red shift of the absorption edge to about 660 nm, corresponding to a narrow bandgap of E_g = 2.0 eV (Fig. 6(b)).

A Mott-Schottky curve of the TiO_2 photoanode (Fig. 6(c)) and an XPS valence band (VB) spectrum for the TpBD powder (Fig. 6(d)) were acquired to calculate the CB potential (E_{CB}) and VB potential (E_{VB}) of the TiO_2 and TpBD semiconductors. By extrapolation of the linear region to C^{-2} = 0, the flat band potential (E_{fb}) of the TiO_2 photoanode can be determined, which is −0.50 V (vs. SCE). Previous studies have demonstrated that the E_{fb} of an n-type semiconductor is ~0.2 V more positive than the E_{CB} value [61]. Therefore, the E_{CB} value of the TiO_2 photoanode is estimated to be −0.70 V (vs. SCE), i.e., −0.46 V (vs. NHE). Accordingly, the E_{VB} value of the TiO_2 photoanode can be obtained, which is 2.74 V (vs. NHE) based on the formula of $E_{VB} = E_{CB} + E_g$. The E_{VB} value of the TpBD powder is 0.90 eV, which is calculated directly by extrapolating a linear fit to the leading edge of the VB XPS spectrum to the baseline. Again, according to the mathematical relationship between E_{VB} and E_{CB} and the foregoing E_g value (2.0 eV), the E_{CB} of the TpBD powder is −1.10 V (vs. NHE). The positive slope in the linear region of the Mott-Schottky curve for the TiO_2/TpBD composite semicon-

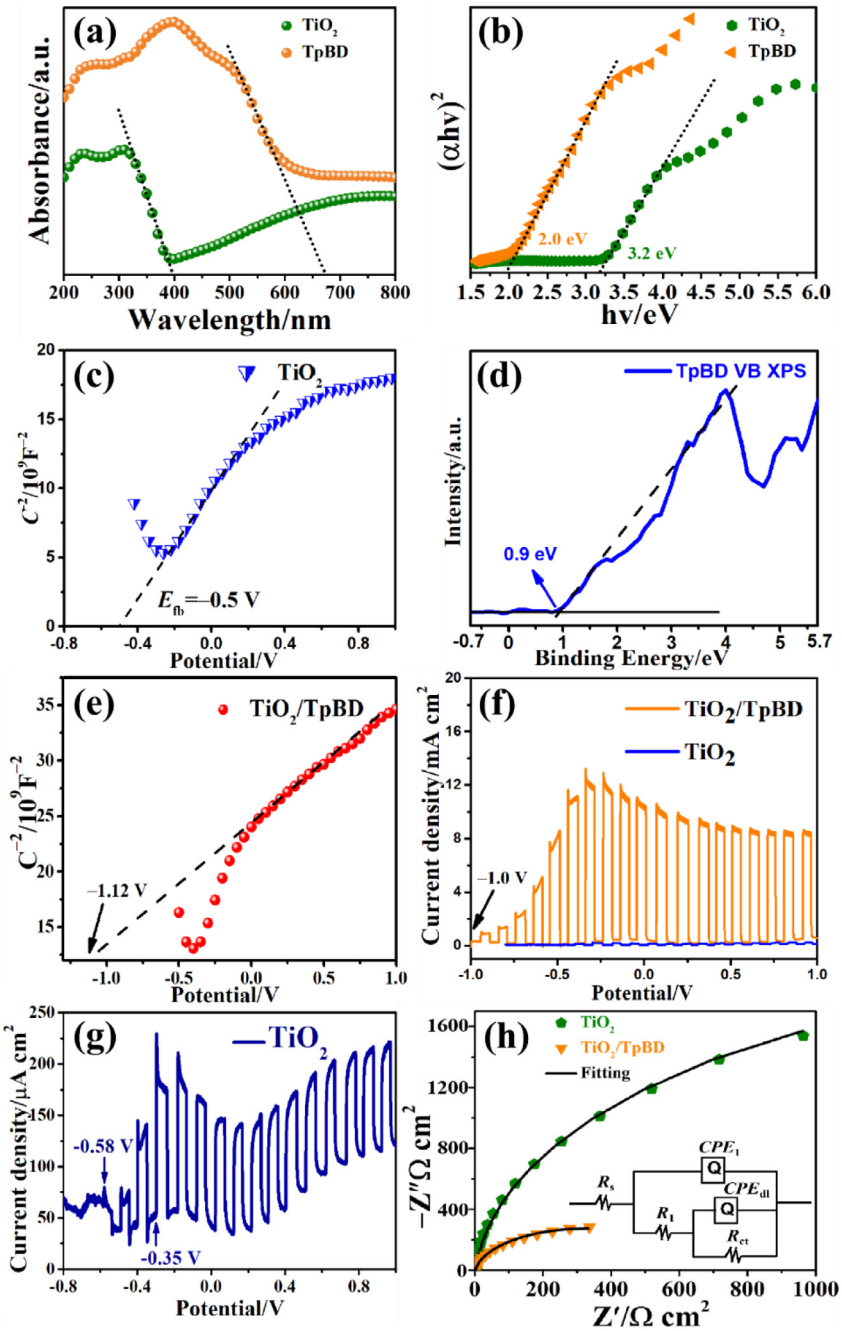

Fig. 6. Photoelectrochemical performance of the TiO_2, TpBD, and TiO_2/TpBD photoelectrodes. (a) UV–vis spectra and (b) plots of $(\alpha hv)^2$ versus hv for the TiO_2 and TpBD photoelectrodes. (c) Mott-Schottky curves of the TiO_2. (d) VB XPS spectrum of TpBD powder. (e) Mott-Schottky curve of the TiO_2/TpBD. (f) The photoinduced variation of the current density over potential (j - E) curves under periodically switching on and off the visible light in 0.1 mol L^{-1} Na_2SO_4 solutions. (g) Enlarged j - E curve for the pure TiO_2 photoelectrode. (h) Nyquist diagram and corresponding EC model for pure TiO_2 and TiO_2/TpBD photoelectrodes in solutions containing 0.1 mol L^{-1} Na_2S and 0.2 mol L^{-1} NaOH.

ductor indicates that the n-type characteristic of the TiO_2 nanotubes remains after deposition of the TpBD film (Fig. 6(e)). The E_{fb} value of the TiO_2/TpBD composite photoanode negatively shifts to −1.12 V (vs. SCE) compared to that of pure TiO_2 photoanode, indicating the increased reduction capability of the photoinduced electrons generated by the TiO_2/TpBD composite [62].

The enhanced photoelectrochemical performance is confirmed by the current density over potential (j - E) curves (Fig. 6(f, g)) and Nyquist diagrams (Fig. 6(h)) of the uncoupled TiO_2 and TiO_2/TpBD photoanodes. The j - E curves of both TiO_2 and TiO_2/TpBD photoanodes under intermittent visible light show obvious photoinduced currents. In the sweeping potential ranging from −1.0 V to 1.0 V (vs. SCE), the photoinduced current of the TiO_2 photoanode is mainly limited to 0.2 mA cm^{-2} including the background current (Fig. 6(g)). In contrast, the current for the TiO_2/TpBD photoanode is enhanced significantly, with a maximum close to 12.0 mA cm^{-2} (Fig. 6(f)). The maximum photoinduced current in the case of the TiO_2/TpBD photoanode is about 60 times higher than that current of the TiO_2 photoanode. The threshold bias potential, a starting point corresponding to generate positive photoinduced current, of the TiO_2/TpBD photoanode is about −1.0 V (vs. SCE), which is much negative in comparison with that of the TiO_2 photoanode

Table 2
The fitted electrochemical parameters based on EIS data of TiO_2 and TiO_2/TpBD photoanodes under visible light.

Samples	R_s/Ω cm^2	CPE_1/S s^n cm^{-2}	R_1/Ω cm^2	CPE_{dl}/S s^n cm^{-2}	R_{ct}/Ω cm^2	χ^2
TiO_2	3.10	6.64×10^{-4}	4.75×10^{2}	1.22×10^{-4}	6.38×10^{3}	2.53×10^{-4}
TiO_2/TpBD	2.87	1.74×10^{-2}	1.8	1.29×10^{-3}	885	2.84×10^{-3}

(around −0.58 V vs. SCE), manifesting that the deposition of the TpBD on the TiO_2 nanotube surface creates a negative movement of the Fermi level. Fig. 6(h) shows the Nyquist plots of the TiO_2 and TiO_2/TpBD photoanodes under visible light illumination and corresponding equivalent circuit (EC) model for fitting (inset at the bottom right corner). In the EC diagram, R_s is the solution resistance, R_1 and CPE_1 represent the resistance and capacitance of the surface film (TiO_2 oxide or both TiO_2 oxide and TpBD deposition), respectively. R_{ct} and CPE_{dl} represent the charge transfer resistance and double-layer capacitance of the electrochemical reactions happening at the solid/electrolyte interface, respectively. The fitted results based on the EC model are listed in Table 2. After depositing TpBD on the TiO_2, the R_1 and R_{ct} decrease from 475 to 1.8 Ω cm^2 and 6380 to 885 Ω cm^2, respectively. The significant decrease of the R_1 and R_{ct} indicates that the movements of both ions in the electrolyte and electrons in the photoelectrode layers become easy, which is beneficial to an acceleration of the electrochemical reactions at the electrode/electrolyte interface and separation of photoinduced electron-hole pairs.

3.3. PECCP performance of the TiO_2/TpBD photoanode to the nickel-coated Mg alloy

To study the PECCP performance of the TiO_2/TpBD photoanode to the Mg/Ni electrode, the j - t (at OCP) and OCP - t curves of the TiO_2 and TiO_2/TpBD photoanodes coupled with the Mg/Ni electrode (denoted by Mg/Ni-TiO_2 and Mg/Ni-TiO_2/TpBD, respectively) under visible light irradiation were obtained. Photocurrent density at OCP is an essential parameter to evaluate the separation efficiency of photo-generated charges. The transient photocurrent curves of the two different photoanodes coupled with the Mg/Ni electrode under intermittent visible light illumination are shown in Fig. 7(a). The current densities increase promptly and decay sharply upon on/off cycles of light illumination in both cases, showing the fast response of photocurrent of the photoanodes to visible light. The curves of the transient photo-generated current show good reproducibility and stability after several cycles of visible light illumination. The TiO_2/TpBD photoanode exhibits a much larger steady photocurrent density (450 μA cm^{-2}), nearly 5.6 times that of the pure TiO_2 photoanode (80 μA cm^{-2}) under visible light irradiation. The fast response and remarkable photocurrent are attributed to the formation of heterojunction structure at the interface between TiO_2 and TpBD, which favors the separation and transfer of the photoinduced electron-hole pairs [63]. The positive photocurrent density exhibits that the photoelectrons flow from the TiO_2/TpBD photoanode to the Mg/Ni electrode through the Cu wire, imparting cathodic polarization and protection for the Mg/Ni electrode.

The photoinduced decrease of the mixed potential of the Mg/Ni electrode coupled with the TiO_2/TpBD photoanode is also an important parameter to assess the charge separation efficiency and the PECCP performance [64]. As shown in Fig. 7(b), the OCP of the Mg/Ni electrode in the dark is −0.38 V before coupling with TiO_2/TpBD photoanode. When the Mg/Ni electrode is coupled with the TiO_2/TpBD photoanode, the OCP moves obviously to a lower value (−0.47 V) even in the dark. After turning on the light, the OCP shifts quickly toward a more negative direction and gradually drops to a very low value. When the lamp is turned off, the OCP instantly shifts with a very slow speed toward a more positive potential and cannot return to the initial potential (−0.47 V) within 100s. Once the visible light is switched on and off again, similar OCP variations are observed. After several on/off cycles, the photoinduced OCP under visible light illumination keeps at about −1.13 V, exhibiting a maximum OCP drop of 660 mV. During the dark periods, the OCP only increases to −0.99 V at most with a relatively slow speed, indicating a degree of electron storage property of the TiO_2/TpBD photoanode. In comparison, the OCP curve of the Mg/Ni electrode coupled with TiO_2 photoanode shows a maximum OCP drop of only 230 mV from −0.45 to −0.68 V. The OCP rapidly increases and returns to the initial value when the light is turned off, indicating the relatively inferior PECCP performance and electron storage capability of the TiO_2 photoanode. The large OCP drop of the Mg/Ni electrode coupled with TiO_2/TpBD photoanode can be maintained for 2 h at least under visible illumination. It can gradually return to its initial potential after turning off the light source (Fig. 7(c)), manifesting good stability and durability of the TiO_2/TpBD photoanode.

To demonstrate the enhanced physical barrier protection of the Ni layer to the Mg alloy substrate with the assistance of the TiO_2/TpBD photoanode, the OCP - t curves of the Mg/Ni electrodes before and after coupling with TiO_2/TpBD photoanode under visible light illumination are measured (Fig. 7(d)). The deposition time of the nickel layer on the Mg alloy is purposefully shortened to 20 min for observation of the galvanic corrosion between Mg substrate and Ni layer within a short period. In the case without coupling with TiO_2/TpBD photoanode, the OCP of the Mg/Ni electrode stabilizes at −0.38 V in the early stage, i.e., the stable potential of nickel in a NaCl solution. After ~35 min of exposure (t_1), the OCP of the Mg/Ni electrode drops sharply to −1.22 V (vs. SCE), meaning occurrence of galvanic corrosion and failure of corrosion protection of the nickel layer to Mg alloy. After coupling with TiO_2/TpBD photoanode under visible light irradiation, the OCP moves negatively and keeps at a low value (−1.12 V) in the early stage. The significant photo-potential (photo-induced OCP) drop in comparison with the OCP of the Mg/Ni electrode without coupling (−0.38 V) demonstrates the injection of abundant photogenerated electrons from the TiO_2/TpBD photoanode to the nickel layer surface, resulting in cathodic polarization and protection of the nickel layer. After 117 min (t_2) of immersion in the NaCl solution, galvanic corrosion also occurs, causing further OCP decrease down to −1.35 V. The slightly decreased OCP in comparison with that without coupling with TiO_2/TpBD photoanode (−1.22 V) indicates the continuous injection of photoelectrons even after the occurrence of galvanic corrosion. However, the photoelectrons are useless in terms of direct or indirect corrosion protection to Mg alloy since the formed mixed potential (−1.35 V) is higher than the E_c of the Mg alloy (−1.50 V). Nevertheless, compared with the case without coupling, the onset of galvanic corrosion is delayed significantly when coupled with TiO_2/TpBD photoanode under illumination. In other words, the physical barrier protection of the nickel layer to the Mg alloy is enhanced with the assistance of the electrons produced by the TiO_2/TpBD photoanode, which is also visually confirmed by the digital photos of the nickel-coated Mg alloy with and without coupling with TiO_2/TpBD photoanode after the same time (108 min) of exposure to NaCl solutions (Insets in Fig. 7(d)). A cavity that is big and deep enough to show the underlying Mg alloy is observed in the photos of the Mg/Ni electrode without coupling with photoanode (photo ①). At the same time, corrosion pits are not found at

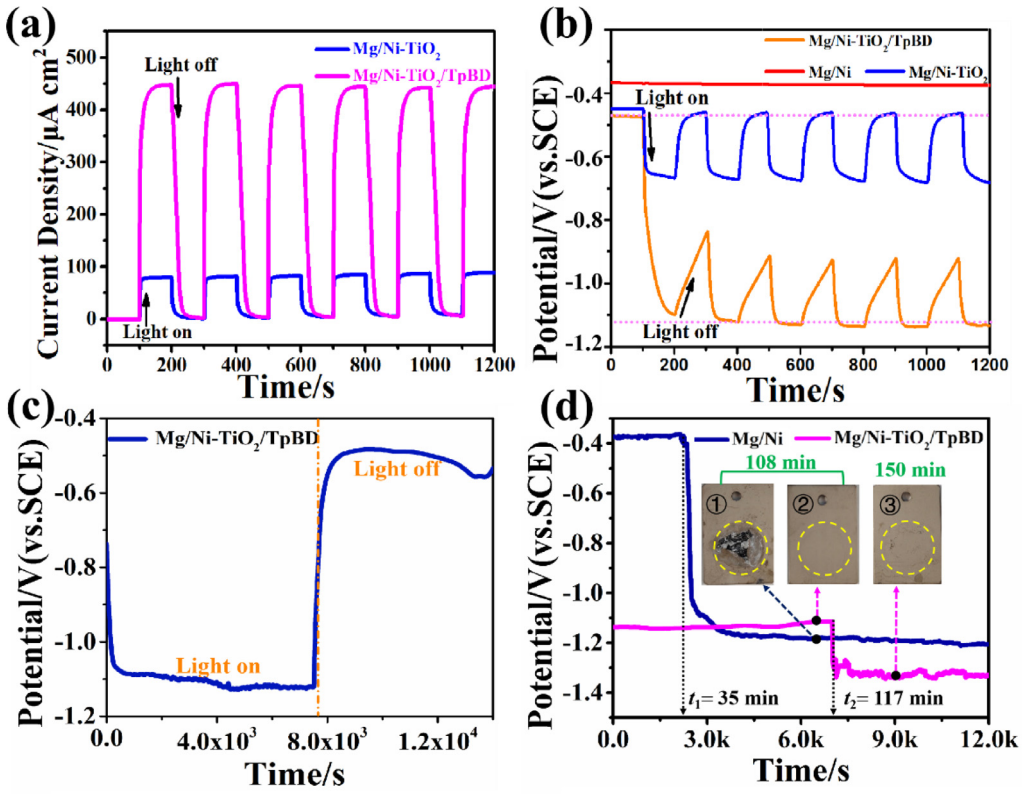

Fig. 7. Time-dependent profiles of the photoinduced (a) current densities and (b) OCP of the uncoupled Mg/Ni electrode and the Mg/Ni working electrode coupled with TiO_2/TpBD photoanode or TiO_2 photoanode under intermittent visible light illumination ($\lambda > 420$ nm). (c) The long-term time-dependent OCP response of the Mg/Ni electrode coupled with TiO_2/TpBD photoanode under visible light irradiation. (d) OCP - t curve of the Mg/Ni electrode (electroless Ni plating time is purposefully decreased to 20 min) with and without coupling with TiO_2/TpBD photoanode under visible light irradiation. The insets in (d) are the digital photos of the Mg/Ni electrodes (①) uncoupled with photoanode after 108 min of exposure to NaCl solutions, and coupled with photoanode after (②) 108 min and (③) 150 min of exposure to NaCl solutions.

Table 3
Fitted EIS parameters for the Mg/Ni electrodes under different conditions in the NaCl solutions.

Samples	R_s/Ω cm^2	CPE$_1$/S s^n cm^{-2}	R_1/Ω cm^2	CPE$_{dl}$/S s^n cm^{-2}	R_{ct}/Ω cm^2	χ^2
Mg/Ni	4.90	4.83×10^{-5}	1.20×10^{3}	2.53×10^{-7}	2.15×10^{4}	1.95×10^{-4}
Mg/Ni- TiO_2/TpBD-dark	7.52	2.26×10^{-5}	1.15×10^{3}	2.26×10^{-3}	2.81×10^{3}	8.52×10^{-5}
Mg/Ni- TiO_2/TpBD-light	5.62	9.90×10^{-5}	1.19×10^{3}	3.87×10^{-2}	171.80	2.08×10^{-5}

the surface of the Mg/Ni electrode in the presence of PECCP (photo ②). With increasing exposure time up to 150 min, the Mg/Ni electrode coupled with TiO_2/TpBD photoanode is only corroded slightly with some corrosion pits and the nickel layer does not peel off from the magnesium alloy substrate (photo ③).

EIS is used to evaluate the PECCP performance of the TiO_2/TpBD photoanode to the Mg/Ni electrode under dark and visible light illumination (Fig. 8). During the EIS test, galvanic corrosion is not observed, suggesting that the corrosive electrolyte does not penetrate the nickel layer to the Mg alloy surface. Previous studies have demonstrated that a passive nickel oxide film will be formed on the nickel film surface when the Mg/Ni electrode is exposed to the NaCl solution [30]. Therefore, an EC diagram (inset in Fig. 8(a)) with two-time constants is used for fitting the EIS data. There are five electrical elements in the model, where R_s represents solution resistance, R_1 and CPE$_1$ (constant phase element) represent the resistance and capacitance of the natural nickel oxide film on the nickel surface, respectively, and R_{ct} and CPE$_{dl}$ represent charge transfer resistance and double-layer capacitance, respectively. The EC model allows for fitting the experimental data with a high goodness of fit and low chi-square less than 2.0×10^{-4} (Table 3). When the Mg/Ni electrode is not coupled with the photoanode (denoted by Mg/Ni), the R_1 and R_{ct} are 1.20 and 21.5 kΩ cm^2, indicating good physical barrier protection of the nickel layer. After coupling with the TiO_2/TpBD photoanode in dark (Mg/Ni-TiO_2/TpBD-dark), the R_1 value changes slightly, but the R_{ct} value decreases by nearly one order of magnitude to 2.81 kΩ cm^2. The decrease in R_{ct} value may be ascribed to the more negative free corrosion potential of the TiO_2/TpBD composite compared with that of the nickel. Therefore, the former is anodically polarized while the nickel is cathodically polarized, facilitating the electrochemical reactions at the solid/electrolyte interface. When the light is turned on (Mg/Ni-TiO_2/TpBD-light), the marginal variation of R_1 value (1.19 kΩ cm^2) indicates that the resistance of the nickel oxide layer is not obviously changed upon coupling and illumination, while compared with that before irradiation, the R_{ct} value further decreases by more than one order of magnitude to 171.8 Ω cm^2, suggesting the transfer of photoelectrons from the photoanode to the nickel surface. The slight change in R_1 and substantial decrease in R_{ct} can be distinguished clearly by the enlarged plots as shown in Fig. 8(b). The diameters of the capacitive loops at high and intermediate frequencies corresponding to the R_1 values remain almost unchanged for the Mg/Ni-TiO_2/TpBD samples before and after illumination. At a low-frequency region, compared with that in the dark, the capacitive loop diameter corresponding to the R_{ct} value decreases remarkably after turning on the light.

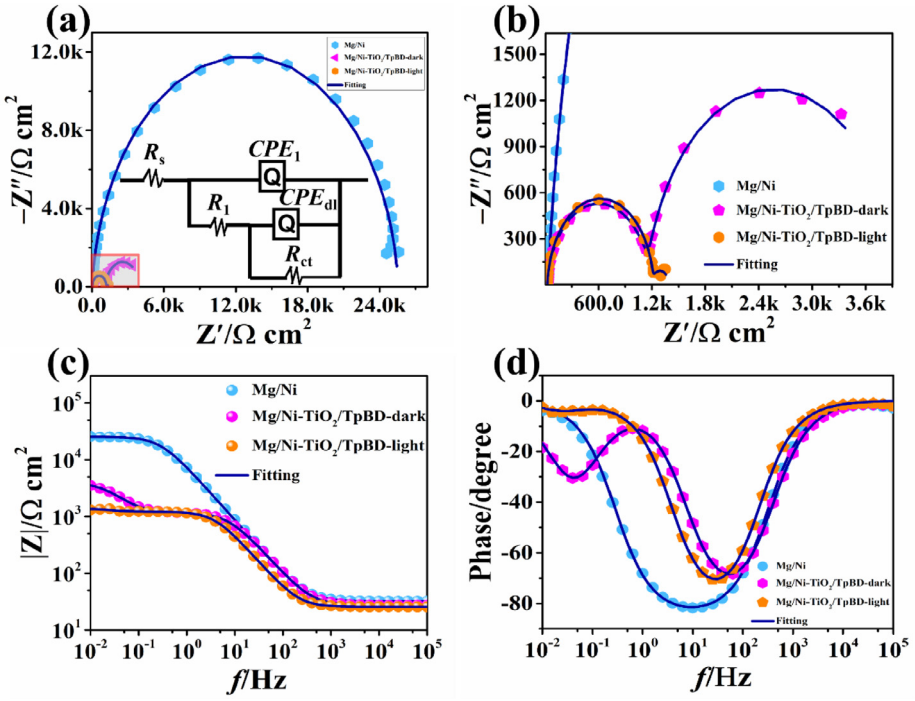

Fig. 8. EIS of the Mg/Ni electrode with and without coupling with TiO_2/TpBD photoanode in a 3.5 wt.% NaCl solution under dark state and visible light irradiation. (a) Nyquist diagram with an inset showing the EC diagram for fitting. (b) An enlarged view of the orange rectangle area in (a). Bode diagrams of (c) modulus versus frequency and (d) phase versus frequency.

Table 4
Electrochemical parameters based on the potentiodynamic polarization curves.

Samples	E_{corr}/ V (vs. SCE)	j_{corr}/ μA cm^{-2}	β_c/ mV dec^{-1}
Mg	−1.50 ± 0.038	7.08 ± 1.14	−490
Mg/Ni	−0.33 ± 0.015	3.43 ± 0.75	−347
Mg/Ni-TiO_2/TpBD-dark	−0.84 ± 0.038	16.4 ± 1.05	−197
Mg/Ni-TiO_2/TpBD-light	−1.12 ± 0.049	69.6 ± 1.72	−190

The significant decrease in R_{ct} value and diameter of the capacitive loop at the low frequencies indicate the good charge transfer capability and effective PECCP property under illuminated condition, which is attributed to the inhibition of charge recombination and facilitation of charge separation arising from the extended light absorption and suitable energy-band matching between TpBD and TiO_2 [39]. The aforementioned obvious decrease in impedance at low-frequency region after illumination and the two time constants characteristic can also be observed easily from the modulus-frequency and phase-frequency diagrams as shown in Fig. 8(c, d). Fig. 8(c) shows that the impedance modulus at 0.01 Hz of the Mg/Ni-TiO_2/TpBD-dark is 1.48 kΩ cm^2, which is much higher than that value of the Mg/Ni-TiO_2/TpBD-light (1.21 kΩ cm^2). The phase angle spectra of the Mg/Ni-TiO_2/TpBD samples, especially for the sample in the dark, clearly reveal two maxima at the intermediate and low frequencies (Fig. 8(d)).

To further confirm the PECCP performance of the TpBD/TiO_2 photoanode, potentiodynamic polarization curves of the Mg alloy, single Mg/Ni electrode in dark state, and Mg/Ni electrodes coupled with TiO_2/TpBD photoanodes both in the dark and under visible light illumination are also measured (Fig. 9). The corresponding electrochemical parameters based on the potentiodynamic polarization curves are tabulated in Table 4. In general, a more positive E_c of a metallic coating reflects better corrosion resistance owing to the lower corrosion tendency from the thermodynamic aspect. It can be found that the E_c and corrosion current density (j_{corr}) of the Mg alloy in a 3.5 wt.% NaCl solution are −1.50 V (vs. SCE) and 7.08 μA cm^{-2}, respectively. In comparison, these values of the uncoupled Mg/Ni electrode are −0.33 V (vs. SCE) and 3.43 μA cm^{-2}, respectively, indicating that the nickel layer can act as a physical barrier and provide good corrosion protection to the Mg alloy in a NaCl electrolyte. After coupling with the TiO_2/TpBD photoanode, the E_c the Mg/Ni electrode decreases to −0.84 V (vs. SCE), and the corresponding j_{corr} increases to 16.4 μA cm^{-2}, indicating that the TiO_2/TpBD photoanode can provide cathodic polarization protection for the Ni layer even in the dark [65]. The E_c of the Mg/Ni electrode further decreases down to −1.12 V (vs. SCE) when the lamp is turned on, resulting in a photoinduced potential drop (280 mV), which agrees well with the results by measuring the OCP variations. In addition, the j_{corr} of the Mg/Ni electrode coupling with TiO_2/TpBD photoanode under visible light illumination (69.6 μA cm^{-2}) is more than four times higher than that in the dark (16.4 μA cm^{-2}), demonstrating the formation of photogenerated charges and transfer of photogenerated electrons to nickel surface to hasten electrochemical reactions. Based on the remarkable E_c difference as high as 0.79 V between the uncoupled and coupled Mg/Ni electrode under illumination and the obvious increase in j_{corr} after irradiation, it can be concluded that the nickel layer on the Mg alloy surface is well protected via cathodic polarization.

3.4. PECCP mechanism of the TiO_2/TpBD photoanode to the nickel-coated Mg alloy

It is necessary to compare the electron density variation of the TpBD before and after growth on the TiO_2 nanotubes and the interfacial charge transfer pathways between the TpBD and TiO_2 to study the PECCP mechanism. The high-resolution XPS spectra of several different elements for the pure TpBD powder are shown in Fig. 10. The C 1s spectrum of the pure TpBD powder can be split into three peaks at binding energies of 284.97 (C=C), 286.4 (C=N), and 288.2 eV (C=O), which shift toward a higher energy region by 0.22, 0.03, and 0.07 eV in comparison with that of the

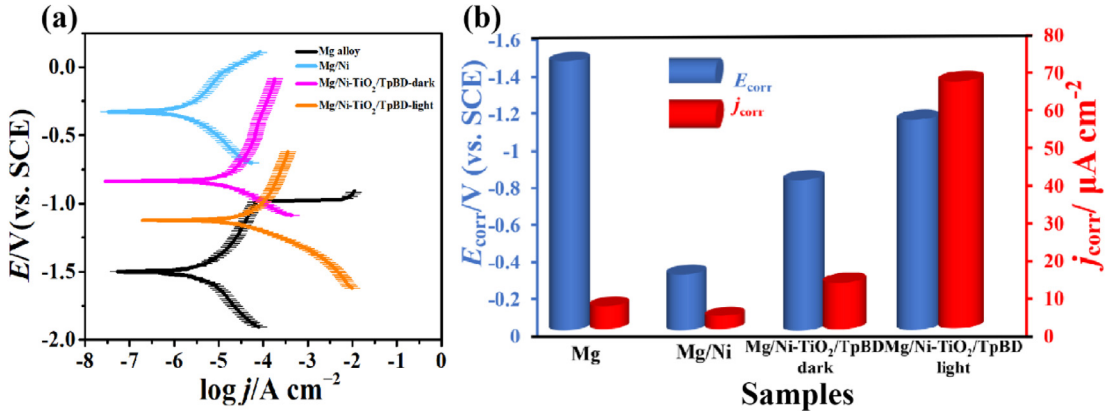

Fig. 9. (a) Potentiodynamic polarization curves of the Mg alloy, single Mg/Ni electrode, and Mg/Ni electrodes coupled with TiO_2/TpBD photoanode in 3.5 wt.% NaCl corrosive mediums in the dark and under visible light illumination. (b) The corresponding E_{corr} and j_{corr} for the samples under different conditions based on the polarization curves.

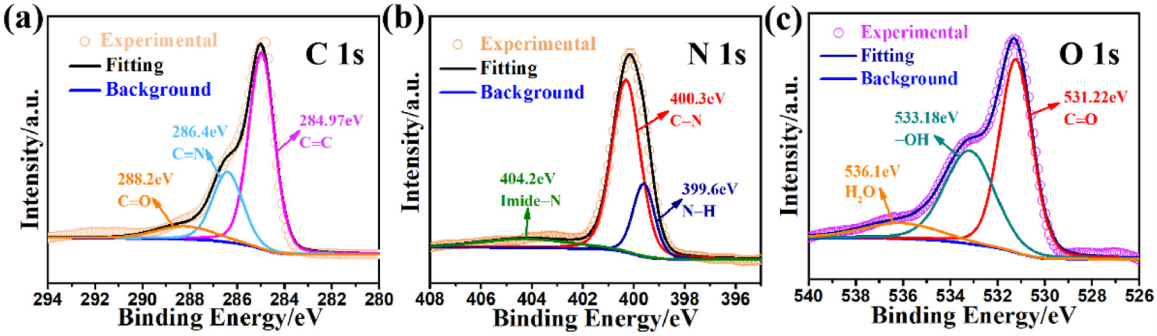

Fig. 10. High-resolution XPS spectra of (a) C 1s, (b) N 1s, and (c) O 1s for the pure TpBD powder.

TiO_2/TpBD composite (Fig. 5(b)), respectively. The N 1s spectrum of the pure TpBD can also be deconvoluted into three different types of nitrogen species, i.e., N–H (399.6 eV), C–N (400.3 eV), and imide-N (404.2 eV), which are correspondingly higher than that of the TiO_2/TpBD composite (Fig. 5(c)). By comparing the O 1s XPS spectra of the pure TpBD with that of the TiO_2/TpBD composite, a similar decrease in binding energies is also observed, namely, a decrease by 0.22 and 0.18 eV from 531.22 (C=O) and 533.18 (−OH) eV for pure TpBD to 531.0 (C=O) and 533.0 (−OH) eV for TiO_2/TpBD composite, respectively (Fig. 5(d) and Fig. 10(c)). These negative shifts in the binding energies suggest the shift of the electron density from TiO_2 to TpBD and an increase in electron density for the TpBD after depositing on the TiO_2 [66], demonstrating the formation of interfacial covalent bonds and the intimate contact between TpBD and TiO_2, which is believed to be beneficial to the generation of a direct Z-scheme heterojunction [67].

Elucidation of the interfacial charge transfer pathway is vital to demonstrate the formation of a direct Z-scheme heterojunction between the TiO_2 and TpBD semiconductors. Therefore, ESR spectra of pure TiO_2, TpBD, and TiO_2/TpBD composite semiconductors for DMPO-·OH in water and DMPO-$\cdot O_2^-$ in methanol under visible light illumination were obtained and are shown in Fig. 11(a, b). It can be seen from the ESR spectra (Fig. 11(a)) that DMPO-·OH signals are weak for pure TpBD and medium for TiO_2, suggesting that the production of hydroxyl radicals (·OH) is limited by the photogenerated holes from VB of TpBD, but enough ·OH can be produced in the case of pure TiO_2. The formation of TiO_2/TpBD composite leads to a significant enhancement of the ·OH signal. Similar results are also observed for the $\cdot O_2^-$ signal (Fig. 11(b)).

To correlate the above experimental results with the photochemical characteristics of the composite materials, we analyzed the alignment of the energy bands at the interface between TpBD and TiO_2. A staggered band structure, forming either a traditional type-II heterojunction or a direct Z-scheme heterojunction, is illustrated in Fig. 12 [68]. In the former case (Fig. 12(a)), when electron and hole pairs are generated by both semiconductors under illumination, the photogenerated electrons on the CB of TpBD semiconductor transfer to the CB of TiO_2 semiconductor, while the photogenerated holes transfer in the opposite direction (i.e., from TiO_2 to TpBD). In the direct Z-scheme heterojunction (Fig. 12(b)), the photogenerated electrons on the CB of TiO_2 tend to directly recombine with the photogenerated holes on the VB of TpBD that has a relatively negative VB potential. The interfacial transfers of the photogenerated electrons occur in opposite directions for type-II heterojunction (from TpBD to TiO_2) and direct Z-scheme heterojunction (from TiO_2 to TpBD). Based on the band energies, the observed difference in ESR spectra is attributed to the lower E_{VB} of TpBD (0.9 eV) and higher E_{VB} of TiO_2 (2.74 eV) as compared to the potential of OH^-/·OH (2.3 eV vs. NHE) [69]. The strongest DMPO-·OH signal as depicted in the case of TiO_2/TpBD composite indicates that the charge transfer is incompatible with type-II heterojunction in which the accumulated h^+ on the VB of TpBD cannot oxidize OH^- to produce considerable ·OH. In other words, the interfacial charge transfer between TiO_2 and TpBD complies with the direct Z-scheme pathway, which is further confirmed by the different signal intensities of the DMPO-$\cdot O_2^-$ in pure TiO_2, TpBD, and TiO_2/TpBD composite, as shown in Fig. 11(b). It can be seen that the accumulated e^- on the CB of both TiO_2 and TpBD can reduce O_2 to $\cdot O_2^-$ due to the smaller potential as compared to that of $O_2/\cdot O_2^-$ (−0.33 eV vs. NHE) [70]. The CB potential of pure TpBD (−1.1 eV vs. NHE) is much lower than that of pure TiO_2 (−0.46 eV vs. NHE), resulting in much stronger DMPO-$\cdot O_2^-$ signal in the TpBD sample. In the case of TiO_2/TpBD composite, owing to the improvement in separation of the photogenerated electron-hole pairs, the reduction

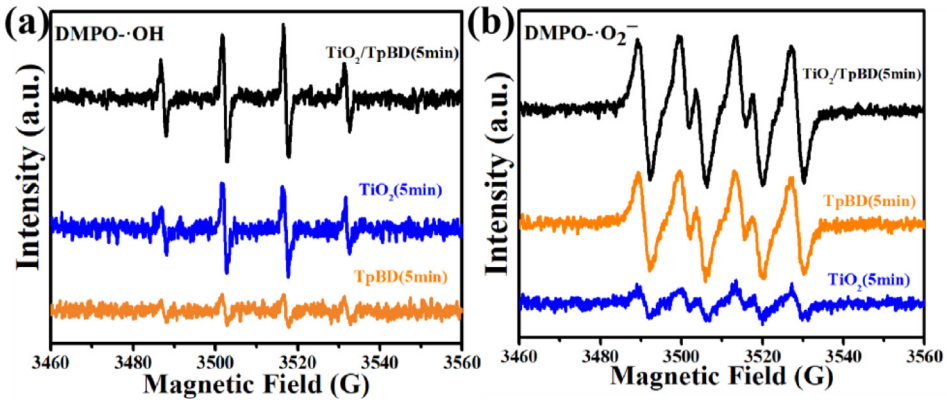

Fig. 11. ESR spectra of pure TiO_2, TpBD, and TiO_2/TpBD composite semiconductors for (a) DMPO-·OH in water and (b) DMPO-·O_2^- in methanol under visible light illumination for 5 min. DMPO: 5, 5-dimethyl-1-pyrroline N-oxide.

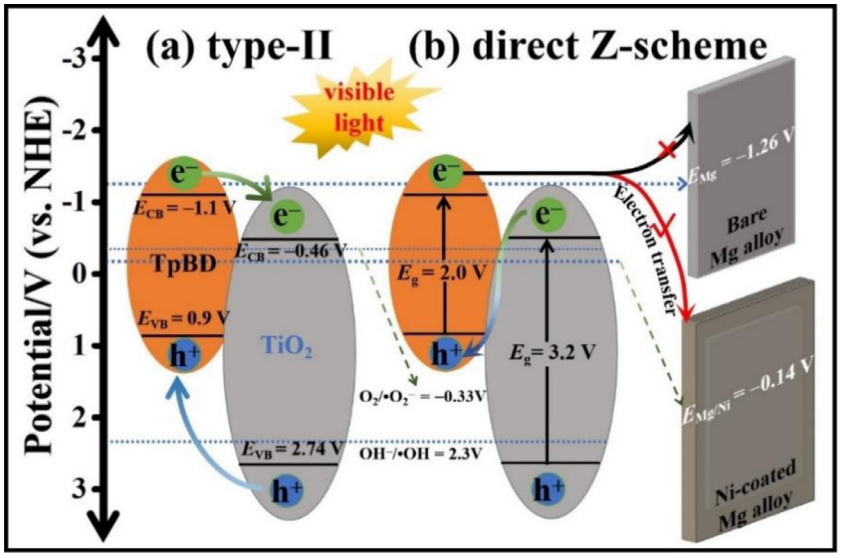

Fig. 12. A schematic illustration of the charge-carrier migration pathways of (a) type-II and (b) direct Z-scheme heterojunctions for the TiO_2/TpBD composite photoanode, along with the transfer of accumulated photogenerated electrons from the CB of the TpBD semiconductor to the nickel-coated magnesium alloy to induce PECCP performance.

ability is enhanced further, showing the strongest DMPO-·O_2^- signal.

The formation of a direct Z-scheme TiO_2/TpBD system is also consolidated by the measurement of OCP variations of the Mg/Ni electrode coupled with a TiO_2 or TiO_2/TpBD photoanode under intermittent visible light illumination (Fig. 7(b)). The photoinduced potential of the Mg/Ni electrode coupled with pure TiO_2 photoanode stabilizes at a value of −0.68 V (vs. SCE), or −0.44 V (vs. NHE), which is very close to the CB potential of TiO_2 (−0.46 V vs. NHE). If the charge-carrier migration mechanism of the TiO_2/TpBD composite complies with type-II heterojunction, the photoinduced potential should also be close to the CB potential of TiO_2 semiconductor. However, the potential of the Mg/Ni electrode coupled with TiO_2/TpBD composite under irradiation stabilizes at a value of −1.13 V (vs. SCE), or −0.89 V (vs. NHE), which is much more negative than the CB potential of TiO_2 and closer to the CB potential of TpBD semiconductor. Thus, the photoinduced potential drop is attributed to the migration of photogenerated electrons from the CB of TpBD semiconductor, rather than that of TiO_2 semiconductor.

Importantly, the formation of a nickel coating on magnesium alloy is shown to play an important role in an effective coupling with the above photochemical characteristics (see right panel of Fig. 12). The photogenerated electrons in the pure TiO_2 and TiO_2/TpBD composite photoanodes cannot undergo upward transfer to the bare magnesium alloy. This is because the CB potentials of the semiconductors are more positive than E_c of the bare magnesium alloy (−1.26 V vs. NHE). For the pristine nickel-coated magnesium alloy, owing to the intact wrap of the coating to the substrate, E_c value shifts remarkably toward a more positive direction to −0.14 V (vs. NHE), which corresponds to E_c value of a nickel-phosphorus coating. In this case, compared to the CB potential of the single TiO_2 photoanode or TiO_2/TpBD composite photoanode, E_c of the nickel-coated magnesium alloy is more positive, thereby the photogenerated electron can migrate to the coating surface. Especially, in the case of TiO_2/TpBD photoanode, the CB potential of the TpBD semiconductor is as low as −1.1 V (vs. NHE). Such a big potential difference between the E_c of the Mg/Ni electrode and the CB potential of the TpBD semiconductor produces enough OCP drop when the Mg/Ni electrode is coupled with the TiO_2/TpBD photoanode under visible light illumination, generating direct PECCP to the nickel coating against corrosion. The direct cathodic polarization protection via TiO_2/TpBD photoanode prolongs the nickel coating's corrosion protection to the underlying magnesium alloy by a more effective physical barrier against corrosive species present in the environment.

4. Conclusions

In summary, the charge transfer process in the TiO_2/TpBD composite system is shown to follow a direct Z-scheme photocatalytic mechanism, which improves the photoelectrochemical performance by coupling TpBD-decorated TiO_2 photoanode with nickel coating on Mg alloy for an effective corrosion protection. Although the accumulated photogenerated electrons on the CB of the TpBD semiconductor are ineffective in transferring to the magnesium alloy for direct corrosion protection, they can effectively transfer to the nickel-coated magnesium alloy surface for PECCP of the nickel coating. This improvement remarkably prolongs corrosion protection of the nickel coating to the magnesium alloy by a physical barrier.

The TiO_2-based composite photoanode, consisting of an anodic oxidized TiO_2 nanotube array underlayer and a hydrothermal deposited covalent organic framework TpBD thin film, is promising for direct PECCP to the nickel interlayer and indirect corrosion protection to the Mg alloy. Compared to the single Mg/Ni electrode in the dark, a large potential drop as high as ~660 mV is obtained after coupling with the TiO_2/TpBD photoanode, suggesting direct PECCP of the composite to the nickel layer. Furthermore, under the assistance of the PECCP, the physical barrier protection time of the nickel layer to the Mg alloy extends to 117 min, which is three times higher than that of the single Mg/Ni electrode without photoanode. The enhanced photoelectrochemical and PECCP performances of the composite photoanode are attributed to the well-matched conduction and VBs between the TiO_2 and TpBD semiconductors to form a direct Z-scheme heterojunction. This promotes an effective spatial separation of carriers and prolongs the lifetime of the photogenerated electrons. These results not only further demonstrate the utilization of a photoanode in direct PECCP to the nickel layer for an indirect corrosion protection of the underlying Mg alloy, but also pave the way for better design of highly efficient photoanode composites.

Acknowledgements

This work has been supported by the Science and Technology Department of Sichuan Province (No. 2021ZYD0049); the Natural Science Foundation of Hunan Province (No. 2021JJ30543); Open Project Program of the State Key Laboratory of Photocatalysis on Energy and Environment (No. SKLPEE-KF201811), Fuzhou University; Open Project of Chemical Synthesis and Pollution Control Key Laboratory of Sichuan Province (No. CSPC202004); and the Fundamental Research Funds of CWNU (No. CXTD2020-1). C.J. Zhong acknowledges the support from the National Science Foundation (No. CHE 2102482). Support from the high-level full-time talents program of Guangdong Provincial People's Hospital (No. KY012021462) is also acknowledged.

Supplementary materials

Supplementary material associated with this article can be found, in the online version, at doi:10.1016/j.jmst.2022.02.049.

References

[1] G.L. Yang, Y.J. Ouyang, Z.H. Xie, Y. Liu, W.X. Dai, L. Wu, Appl. Surf. Sci. 558 (2021) 149840.
[2] Y.Y. Bu, J.P. Ao, Green Energy Environ 2 (2017) 331–362.
[3] Z. Song, Z.H. Xie, Micron 112 (2018) 69–83.
[4] H. Li, Y.J. Qiang, W.J. Zhao, S.T. Zhang, Corros. Sci. 191 (2021) 109715.
[5] H. Yan, X. Fan, M. Cai, S. Song, M. Zhu, J. Colloid Interf. Sci. 602 (2021) 131–145.
[6] Y.J. Tarzanagh, D. Seifzadeh, Z. Rajabalizadeh, A. Habibi-Yangjeh, A. Khodayari, S. Sohrabnezhad, Surf. Coat. Tech. 380 (2019) 125038.
[7] Y.J. Zhang, T. Li, B.J. Dou, X.j. Cui, T.W. Shao, Q. Han, Surf. Tech. 50 (2021) 304–312.
[8] M.L. Yang, J.H. Wu, D.Q. Fang, B. Li, Y. Yang, J. Mater. Sci. Technol. 34 (2018) 2464–2471.
[9] S.S. Chen, P. Wan, B.C. Zhang, E. Erişen.Deniz, H. Yang, K. Yang, J. Mater. Sci. Technol. 35 (2019) 19–22.
[10] R. Maurya, A.R. Siddiqui, P.K. Katiyar, K. Balani, J. Mater. Sci. Technol. 35 (2019) 1767–1778.
[11] P. Zhou, L.X. Yang, Y.J. Hou, G.Q. Duan, B.X. Yu, X.J. Li, Y.F. Zhai, B. Zhang, T. Zhang, F.H. Wang, Corros. Commu. 1 (2021) 47–57.
[12] S.J. Liao, B.X. Yu, X.L. Zhang, X.P. Lu, P. Zhou, C.Y. Zhang, X.B. Chen, T. Zhang, F.H. Wang, J. Magnes. Alloy. 9 (2021) 505–519.
[13] Z.Q. Zhang, R.C. Zeng, W. Yan, C.G. Lin, L. Wang, Z.L. Wang, D.C. Chen, J. Alloy. Compd. 821 (2020) 153515.
[14] J. Chen, Y.W. Song, D.Y. Shan, E.H. Han, J. Mater. Sci. Technol. 31 (2015) 384–390.
[15] L.T. Guo, C.D. Gu, J. Feng, Y.B. Guo, Y. Jin, J.P. Tu, J. Mater. Sci. Technol. 37 (2020) 9–18.
[16] X.L. Fan, C.Y. Li, Y.B. Wang, Y.F. Huo, S.Q. Li, R.C. Zeng, J. Mater. Sci. Technol. 49 (2020) 224–235.
[17] R. Fang, R.J. Liu, Z.H. Xie, L. Wu, Y.J. Ouyang, M.Q. Li, Surf. Coat. Tech. 432 (2022) 128054.
[18] L.J. Fan, W.X. Sun, Y.H. Zou, Q.Q. Xu, R.C. Zeng, J.R. Tian, J. Mater. Sci. Technol. 111 (2022) 167–180.
[19] L. Wu, X.X. Ding, Z.C. Zheng, A.T. Tang, G. Zhang, A. Atrens, F.S. Pan, J. Mater. Sci. Technol. 64 (2021) 66–72.
[20] J. Chen, L. Wu, X.X. Ding, Q. Liu, X. Dai, J.F. Song, B. Jiang, A. Atrens, F.S. Pan, J. Mater. Sci. Technol. 64 (2021) 10–20.
[21] X. Wang, L.X. Li, Z.H. Xie, G. Yu, Electrochim. Acta. 283 (2018) 1845–1857.
[22] T. Hu, Y.J. Ouyang, Z.H. Xie, L. Wu, J. Mater. Sci. Technol. 92 (2021) 225–235.
[23] Y.J. Ouyang, L.X. Li, Z.H. Xie, L.L. Tang, F.H. Wang, C.J. Zhong, J. Magnes. Alloy. 10 (2022) 836–849.
[24] Z.H. Xie, Y. Shu, T. Hu, J. Mater. Eng. 49 (2021) 70–76.
[25] L.X. Li, Z.H. Xie, C. Fernandez, L. Wu, D.J. Cheng, X.H. Jiang, C.J. Zhong, Electrochim. Acta 330 (2020) 135186.
[26] Y.H. Cao, D.J. Zheng, F. Zhang, J.S. Pan, C.J. Lin, J. Mater. Sci. Technol. 102 (2022) 232–263.
[27] Y.Q. Li, Y.J. Ouyang, R. Fang, X. Jiang, Z.H. Xie, L. Wu, J. Long, C.J. Zhong, Chem. Eng. J. 430 (2022) 132776.
[28] C. Liu, X.P. Lu, Y. Li, Q.Q. Chen, T. Zhang, F.H. Wang, J. Alloy. Compd. 870 (2021) 159462.
[29] Q. Han, Y. Li, X.P. Lu, D. Mei, Q.Q. Chen, T. Zhang, F.H. Wang, Mater. Lett. 293 (2021) 129731.
[30] R. Gan, D.M. Wang, Z.H. Xie, L. He, Corros. Sci. 123 (2017) 147–157.
[31] D. Li, F. Chen, Z.H. Xie, S.Y. Shan, C.J. Zhong, J. Alloy. Compd. 705 (2017) 70–78.
[32] Z.H. Xie, S.Y. Shan, J. Mater. Sci. 53 (2017) 3744–3755.
[33] A. Gupta, C. Srivastava, Scripta. Mater. 196 (2021) 113763.
[34] D.H. Xia, C.M. Deng, D. Macdonald, S. Jamali, D. Mills, J.L. Luo, M.G. Strebl, M. Amiri, W.X. Jin, S.Z. Song, W.B. Hu, J. Mater. Sci. Technol. 112 (2022) 151–183.
[35] R. Kotoka, S. Yarmolenko, D. Pai, J. Sankar, J. Mater. Sci. Technol. 31 (2015) 873–880.
[36] B. Tan, B. Xiang, S. Zhang, Y. Qiang, L. Xu, S. Chen, J. He, J. Colloid Interf. Sci. 582 (2021) 918–931.
[37] Z.H. Xie, D. Li, Z. Skeete, A. Sharma, C.J. Zhong, ACS Appl. Mater. Inter. 9 (2017) 36247–36260.
[38] K. Qian, W.Z. Li, X.P. Lu, X.X. Han, Y. Jin, T. Zhang, F.H. Wang, J. Magnes. Alloy. 8 (2020) 1328–1340.
[39] S.Y. Guo, L. Chi, T.J.Zhao Feng, Y.B. Nan, X. Sun, Y.L. Huang, B.R. Hou, X.T. Wang, Electroanal. Chem. 880 (2021) 114915.
[40] B.W. Chen, H. Wu, R.B.Yi Liu, W.H. Wang, H.D. Xu, S.X. Zhang, H.Z. Peng, J.W. Ma, H.M. Jiang, R. Zan, S. Qiao, Y. Sun, P. Hou, P. Han, J.H. Ni, X.N. Zhang, J. Mater. Sci. Technol. 52 (2020) 83–88.
[41] J.H. You, Y. Zhao, L. Wang, W.T. Bao, J. Clean. Prod. 291 (2021) 125822.
[42] S. Kandambeth, K. Dey, R. Banerjee, J. Am. Chem. Soc. 141 (2019) 1807–1822.
[43] Z. Lei, Q. Yang, Y. Xu, S. Guo, W. Sun, H. Liu, L.P. Lv, Y. Zhang, Y. Wang, Nat. Commun. 9 (2018) 576.
[44] C.L. Wang, W. Gao, N.Z. Liu, Y. Xin, X.Y. Liu, X.T. Wang, Y. Tian, X.W. Chen, B.R. Hou, Corros. Sci. 176 (2020) 108920.
[45] S. Kandambeth, A. Mallick, B. Lukose, M.V. Mane, T. Heine, R. Banerjee, J. Am. Chem. Soc. 134 (2012) 19524–19530.
[46] Q. Xu, S. Tao, Q. Jiang, D. Jiang, J. Am. Chem. Soc. 140 (2018) 7429–7432.
[47] B.P. Biswal, S. Chandra, S. Kandambeth, B. Lukose, T. Heine, R. Banerjee, J. Am. Chem. Soc. 135 (2013) 5328–5331.
[48] Y.W. Peng, W.K. Wong, Z.G. Hu, Y.D. Cheng, D.Q. Yuan, S.A. Khan, D. Zhao, Chem. Mater. 28 (2016) 5095–5101.
[49] W. Zhao, J. Qiao, T.L. Ning, X.K. Liu, Chin. J. Polym. Sci. 36 (2017) 1–7.
[50] W.B. Tsai, J.Y. Kao, T.M. Wu, W.T. Cheng, J Nanopart 2016 (2016) 1–9.
[51] M. Faheem, S. Aziz, X.F. Jing, T.T. Ma, J.Y. Du, F.X. Sun, Y.Y. Tian, G.S. Zhu, J. Mater. Chem. A 7 (2019) 27148–27155.
[52] A.P. Cote, A.I. Benin, N.W. Ockwig, M. O'Keeffe, A.J. Matzger, O.M. Yaghi, Science 310 (2005) 1166–1170.
[53] E.R. Garcia, R.L. Medina, M.M. Lozano, I. Hernandez Perez, M.J. Valero, A.M.M. Franco, Materials (Basel) 7 (2014) 8037–8057.
[54] Q. Sun, B. Aguila, L.D. Earl, C.W. Abney, L. Wojtas, P.K. Thallapally, S. Ma, Adv. Mater. 30 (2018) e1705479.
[55] W.Q. Fan, X.Q. Yu, H.C. Lu, H.Y. Bai, C. Zhang, W.D. Shi, Appl. Catal. B-Environ. 181 (2016) 7–15.

[56] X. Yang, J. Wang, W. Wang, S. Zhang, C. Wang, J. Zhou, Z. Wang, Mikrochim. Acta. 186 (2019) 145.
[57] Y. Li, M. Zhang, X. Guo, R. Wen, X. Li, X. Li, S. Li, L. Ma, Nanoscale. Horiz. 3 (2018) 205–212.
[58] D.B. Shinde, G. Sheng, X. Li, M. Ostwal, A.H. Emwas, K.W. Huang, Z. Lai, J. Am. Chem. Soc. 140 (2018) 14342–14349.
[59] X. Kang, X.W. Wu, X. Han, C. Yuan, Y. Liu, Y. Cui, Chem. Sci. 11 (2020) 1494–1502.
[60] C. Feng, Z.Y. Chen, J.P. Jing, M.M. Sun, G.Y. Lu, J. Tian, J. Hou, Corros. Sci. 166 (2020) 1455–1466.
[61] Y. Xiao, Y. Qi, X. Wang, X. Wang, F. Zhang, C. Li, Adv. Mater. 30 (2018) e1803401.
[62] Y.Y. Bu, Z.Y. Chen, J.P. Ao, J. Hou, M.X. Sun, J. Alloy. Compd. 731 (2018) 1214–1224.
[63] Y. Bu, Z. Chen, W. Li, B. Hou, ACS Appl. Mater. Inter. 5 (2013) 12361–12368.
[64] J.P. Jing, M.M. Sun, Z.Y. Chen, J.R. Li, F.L. Xu, L.K. Xu, J. Electrochem. Soc. 164 (2017) C822–C830.
[65] H. Li, X.T. Wang, Y. Liu, B.R. Hou, Corros. Sci. 82 (2014) 145–153.
[66] J. Low, B. Dai, T. Tong, C. Jiang, J. Yu, Adv. Mater. 31 (2019) e1802981.
[67] W.L. Yu, D.F. Xu, T.Y. Peng, J. Mater. Chem. A 3 (2015) 19936–19947.
[68] Q.L. Xu, L.Y. Zhang, B. Cheng, J.J. Fan, J.G. Yu, Chem 6 (2020) 1543–1559.
[69] J. Jin, J. Yu, D. Guo, C. Cui, W. Ho, Small 11 (2015) 5262–5271.
[70] H. Wang, B. Zhang, F. Zhao, B. Zeng, ACS Appl. Mater. Inter. 10 (2018) 35281–35288.